

RESEARCH ARTICLE | JANUARY 30 2023

## Dual frequency ultrasonic cavitation in various liquids: High-speed imaging and acoustic pressure measurements

Special Collection: [Cavitation](#)

Justin A. Morton ; Mohammad Khavari ; Abhinav Priyadarshi ; Amanpreet Kaur; Nicole Grobert; Jiawei Mi; Kyriakos Porfyrakis; Paul Prentice ; Dmitry G. Eskin ; Iakovos Tzanakis 



*Physics of Fluids* 35, 017135 (2023)

<https://doi.org/10.1063/5.0136469>




View  
Online



Export  
Citation

CrossMark



### APL Quantum

Bridging fundamental quantum research with technological applications

## Now Open for Submissions

No Article Processing Charges (APCs) through 2024

**Submit Today**

 AIP  
Publishing

# Dual frequency ultrasonic cavitation in various liquids: High-speed imaging and acoustic pressure measurements

Cite as: Phys. Fluids **35**, 017135 (2023); doi: 10.1063/5.0136469

Submitted: 26 November 2022 · Accepted: 7 January 2023 ·

Published Online: 30 January 2023



View Online



Export Citation



CrossMark

Justin A. Morton,<sup>1,a)</sup> Mohammad Khavari,<sup>2</sup> Abhinav Priyadarshi,<sup>1</sup> Amanpreet Kaur,<sup>1</sup> Nicole Grobert,<sup>3</sup> Jiawei Mi,<sup>4</sup> Kyriakos Porfyrakis,<sup>5</sup> Paul Prentice,<sup>6</sup> Dmitry G. Eskin,<sup>7</sup> and Iakovos Tzanakis<sup>1,3,a)</sup>

## AFFILIATIONS

<sup>1</sup>School of Engineering, Computing and Mathematics, Oxford Brookes University, College Ct, Wheatley, Oxford OX33 1HX, United Kingdom

<sup>2</sup>School of Computing and Engineering, College of Science and Engineering, University of Derby, Derby DE22 3AW, United Kingdom

<sup>3</sup>Department of Materials, University of Oxford, Parks Road, Oxford OX1 3PH, United Kingdom

<sup>4</sup>Department of Engineering, University of Hull, Cottingham Road, Hull HU6 7RX, United Kingdom

<sup>5</sup>Faculty of Engineering and Science, University of Greenwich, Central Avenue, Chatham Maritime, Kent ME4 4TB, United Kingdom

<sup>6</sup>Cavitation Laboratory, School of Engineering, University of Glasgow, University Avenue, Glasgow G128QQ, United Kingdom

<sup>7</sup>Brunel Centre for Advanced Solidification Technology, Brunel University London, Kingston Lane, London UB8 3PH, United Kingdom

**Note:** This paper is part of the special topic, Cavitation.

**a)** Authors to whom correspondence should be addressed: 18096707@brookes.ac.uk. Tel.: +44 7747573664 and itzanakis@brookes.ac.uk

## ABSTRACT

Ultrasonic cavitation is used in various processes and applications, utilizing powerful shock waves and high-speed liquid jets generated by the collapsing bubbles. Typically, a single frequency source is used to produce the desired effects. However, optimization of the efficiency of ultrasound reactors is necessary to improve cavitation activity in specific applications such as for the exfoliation of two dimensional materials. This research takes the next step to investigate the effect of a dual frequency transducer system on the bubble dynamics, cavitation zone, pressure fields, acoustic spectra, and induced shock waves for four liquids with a range of physical properties. Using ultra-high-speed imaging and synchronized acoustic pressure measurements, the effect of ultrasonic dual frequencies on bubble dynamics was investigated. The addition of a high frequency transducer (1174 kHz) showed that the bubble fragments and satellite bubbles induced from a low frequency transducer (24 kHz) were able to extend their lifecycle and increase spatial distribution, thus, extending the boundaries of the cavitation zone. Furthermore, this combination of ultrasonic frequencies generated higher acoustic pressures (up to 180%) and enhanced the characteristic shock wave peak, indicating more bubble collapses and the generation of additional shock waves. The dual frequency system also enlarged the cavitation cloud size under the sonotrode. These observations specifically delineated the enhancement of cavitation activity using a dual frequency system pivotal for optimization of existing cavitation-based processing technologies.

© 2023 Author(s). All article content, except where otherwise noted, is licensed under a Creative Commons Attribution (CC BY) license (<http://creativecommons.org/licenses/by/4.0/>). <https://doi.org/10.1063/5.0136469>

## I. INTRODUCTION

Ultrasound and acoustic cavitation is used for a wide variety of industrial applications, such as sonochemistry,<sup>1–4</sup> medical therapy,<sup>5–7</sup> cleaning,<sup>8,9</sup> fragmentation,<sup>10</sup> and more recently utilized in liquid phase exfoliation for the production of two dimensional (2D)

nanomaterials.<sup>11–13</sup> Acoustic cavitation is associated with the formation of bubbles and bubbly clouds that upon implosion release shock waves (SWs) and liquid jets.<sup>14</sup> In particular, SW emissions are inherently powerful, propagating with large velocities and forming large pressure fields in the bulk liquid.

The development and characterization of these SWs are also of importance. For instance, the optimization of SW generation can facilitate exfoliation of layered materials<sup>15</sup> or be used to understand and prevent fatigue and fragmentation of metallic compounds.<sup>10</sup> Analysis of these acoustic emissions is often recorded using acoustic sensors such as a hydrophone where cavitation intensity is resolved and acoustic pressures are measured.<sup>1,16,17</sup> Additionally, SWs from bubble implosions have been shown to generate a specific peak ( $\sim 3.3$  MHz) on the acoustic spectrum,<sup>18</sup> which can be used to resolve and map the spatiotemporal evolution of SW events. This has the potential to control and monitor any ultrasonic cavitation process. For example, during ultrasonic-assisted liquid phase exfoliation, acoustic spectra capture the SW peak development in real-time, indicating graphene generation (i.e., the sharpening of the peak being indicative of graphite exfoliation).<sup>19</sup> Furthermore, the addition of another ultrasound source an order of frequency different has been shown to greatly benefit the exfoliation process, generating tiny bubbles (a few micrometers in size) that have the potential to promote a gentler exfoliation (a less intense cavitation regime that promotes exfoliation via vigorously oscillating bubbles in the vicinity<sup>20</sup> or in-between the flakes<sup>15</sup> imposing a layer fatigue exfoliation effect) and improving the quality, size, and yield of the produced graphene flakes.<sup>19</sup>

However, the addition of multiple-frequency sources increases the complexity of cavitation bubble dynamics hampering their optimization. Understanding the multiple-frequency sound field and corresponding acoustic pressures is pivotal for advancing existing cavitation reactors tailored to specific applications. In accordance to this challenge, there are only a few studies using a dual frequency (DF) source that has been seen to enhance acoustic cavitation based on the increased subharmonic emissions (associated with inertial cavitation) and sonoluminescence intensities.<sup>21,22</sup> Dual acoustic sources have also been shown to enhance metal leaching rates and the final recovery metal extraction values,<sup>23</sup> as well as enhancing sono-chemical degradation of pentachlorophenol.<sup>24</sup>

In line with these studies, we have previously reported that the combination of a 20 and a 1174 kHz source significantly enhances the production of high-quality nanomaterials.<sup>19</sup> The hypothesis is that the combination of different size cavitation bubbles can further increase the cavitation activity while providing a gentler exfoliation in a DF mode. Hence, this work, and in conjunction with the results in Ref. 19, intends to understand the effect the DF processing has on the cavitation dynamics in four different liquids, namely, de-ionized water (DIW), ethanol (EtOH), de-ionized water mixed with ethanol (in a 1:1 ratio; DIW:EtOH), and glycerol, and to elucidate the governing cavitation mechanisms. The choice of these liquids was made based on previous fundamental research<sup>25</sup> and on the fact that their physical properties largely vary (refer to the [supplementary material](#), Table S1) while also previously seen to be suitable for exfoliation of graphene.<sup>26,27</sup> It is well documented that improving exfoliation efficiency and quality depends on further analysis of solvent selection and cavitation behavior, which changes with the characteristic properties of liquids.<sup>28–30</sup> Previous research<sup>25–27,31,32</sup> provides the foundation to expect that cavitation dynamics and SW propagation may vary distinctly due to significantly different density, surface tension, viscosity, vapor pressure, and speed of sound in the studied liquids. The results of this work can be applied to a wider range of dual frequency sonoprocesses where different properties are required, such as

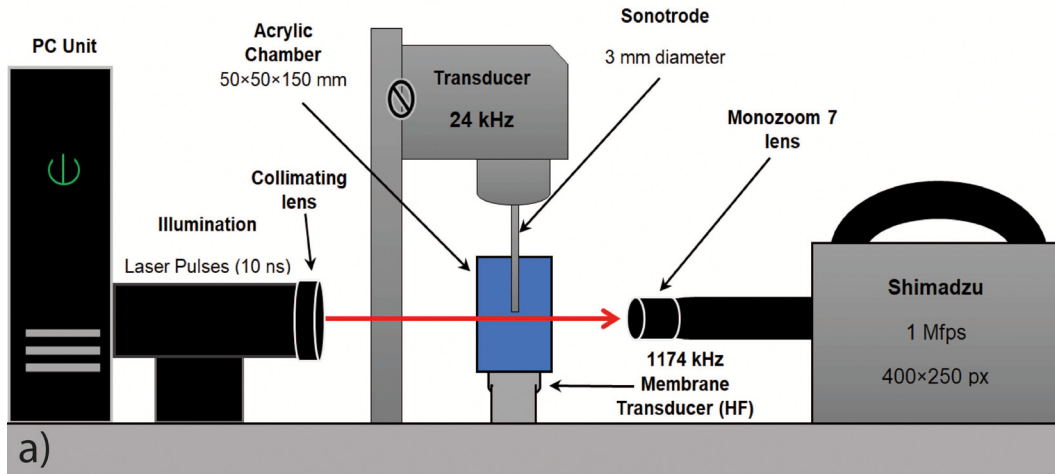
emulsification,<sup>33</sup> sonochemical synthesis,<sup>34,35</sup> in clinical practice,<sup>36</sup> and most notably the exfoliation of 2D nanomaterials.<sup>27</sup> Experiments were conducted for two frequency setups: a low frequency (LF) sonotrode (24 kHz) and a DF system consisting of both the LF sonotrode and a HF transducer membrane (1174 kHz), i.e., 24 + 1174 kHz. Bubble dynamics and the cavitation zone were investigated for each case using ultra-high-speed shadowgraphic camera footage, followed by synchronized high-speed camera imaging in conjunction with acoustic data acquisition measurements recorded using a fiber-optic hydrophone (FOH). These experiments captured *in situ* high-speed imaging and acoustic pressure/spectra to produce a full picture of the cavitation activity. The results revealed that using the DF system cavitation is enhanced, increasing the cavitation zone and density of bubbles for all liquids. Additionally, DF setups produced larger acoustic pressures. The findings of this research may lead to optimizing DF applications, in addition to further understanding the mechanics involved in multi-frequency cavitation bubble interactions.

## II. METHODOLOGY

A multifrequency membrane transducer (Meinhardt Ultrasonics) with a 50 mm titanium diaphragm was used as a HF (operational frequency of 1174 kHz) source for this study. It should be noted here that this particular frequency was found to be the most suitable in a combi-mode for exfoliation of nanomaterials.<sup>19</sup> A custom-made attachment was used converting the 50 mm circular diameter base into an acrylic rectangular chamber ( $5 \times 5 \times 15$  cm<sup>3</sup>) for high-speed camera observations during sonication (i.e., to prevent refraction of light invalidating video recordings) [Fig. 1(a)]. The chamber was filled with either 200 ml of DIW (hexcel chemicals), EtOH, DIW:EtOH (1:1), or glycerol (99.9%, Merck Life Sciences). Next, a Hielscher UP200S transducer (operational frequency of 24 kHz) with a 3 mm diameter (to allow clear observations and fit within the camera field of view) titanium sonotrode was lowered into the chamber  $\sim 8$  cm above from the HF membrane. Experiments were conducted for two scenarios: the LF sonotrode exclusively and the HF membrane combined with the LF sonotrode to form a DF setup (note that HF setup as a scenario is excluded because using only the transducer membrane generates a weak cavitation development as well as being insufficient for exfoliation).

Acoustic pressure measurements were taken using a FOH (Precision Acoustics Ltd) for each case of LF and the DF setups, for each liquid. The LF source was set to input powers of 20%, 60%, and 100% in order to introduce a range of acoustic emissions into the liquids. It is worth noting that each of the transducer input powers is measured in percentage of the maximum power and reflects a certain level of amplitude that is maintained by the transducer. This provided a range of cavitation development and SW generation variation. This variation of acoustic intensity (shown in Fig. 2 caption for each respective liquid and also calculated in the [supplementary material](#), Table S2) is also an important factor for exfoliation of layered materials and helps to optimize the facilitation of nanosheets production. DF measurements used the same input powers with the HF source set at 50% input power. The sensor was positioned  $\sim 5$  mm away from the sonotrode tip and  $\sim 75$  mm above the membrane [Fig. 1(b)]. The FOH was calibrated between 1 and 30 MHz enabling the detection of SWs generated by bubble implosion<sup>25</sup> (a sensitivity plot can be found in the [supplementary material](#) Fig. S1). A bandpass filter was applied to

## Detection of Shockwaves and Standing Waves



## Elucidate Acoustic Emissions and Bubble Dynamics

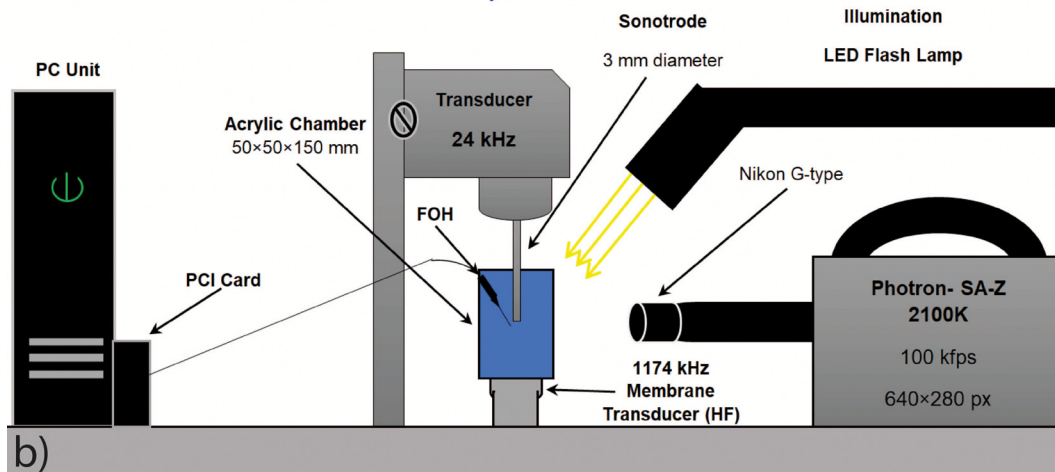


**FIG. 1.** (a) Schematic of the chamber dimensions, transducer membrane, sonotrode, and high-speed imaging setup. The laser illumination passed through the chamber walls and into the camera lens where the image was then resolved and processed on the PC unit. (b) The same schematic using a Photron camera instead for high-speed imaging, and illumination provided by a powerful LED flashlamp. A FOH connected to a PCI card collected acoustic measurements, synchronized with high-speed imaging.

disregard everything outside the calibration range and below 1 MHz. Fast Fourier transform was used to deconvolute and convert the hydrophone output voltage to spectra, where the root means square pressure ( $P_{RMS}$ ) and maximum pressure ( $P_{max}$ ) were calculated. The  $P_{RMS}$  pressure measurements take into account all the associated acoustic emissions, whereas  $P_{max}$  measures the maximum acoustic pressure from each waveform and then averages over the total number of waveforms. As the FOH is primed to detect SWs (which are generally responsible for generating the largest acoustic emissions), the  $P_{max}$  plots are indicative of the inertial cavitation contribution. Data were recorded from 60 waveforms of cavitating emission signals using a 2 ms time period and averaged for each case. During the process, intrinsic background noise was removed from the initial voltage signal. A step by step procedure on the calibration, signal processing and pressures conversion can be found elsewhere.<sup>18,37</sup>

High-speed shadowgraphic imaging was performed using a Shimadzu (HPV X2) camera capturing at  $1 \times 10^6$  frames per second (fps) [Fig. 1(a)]. The combination of using laser illumination with this large frame rate elucidates high resolution images able to capture the formation of standing waves and SW propagation (as previously demonstrated in Ref. 15). Each sequence recorded 265 frames with a resolution of  $400 \times 250$  pixels. For illumination, 10 ns synchronized laser pulses through a collimating lens were used (CAVILUX Smart UHS system), providing effective temporal resolution to observe the generated SWs. More information on this experimental arrangement can be found elsewhere.<sup>15</sup>

Finally, a Peripheral Component Interconnect (PCI) card was installed into the PC to conduct synchronization of the high-speed imaging and acoustic pressure measurements [Fig. 1(b)].<sup>26</sup> A Photron-SA-Z 2100K camera was used at a frame rate of 100 000 fps over

640 × 280 pixels. This setup provided the capability to capture longer duration recordings of cavitation events occurring in the liquids. The camera resolution was 12.7  $\mu\text{m}$  per pixel with a shutter speed of 8.39  $\mu\text{s}$ . For illumination, a light beam LED flashlamp (GS Vitec) was positioned by the container.

### III. RESULTS AND DISCUSSION

#### A. Acoustic pressure measurements and spectra

Acoustic pressure plots of LF and DF setups are shown in Fig. 2. It is apparent that the addition of the HF membrane (in DF) increased

the cavitation intensity (measured in the range of 1–30 MHz) in each liquid for the majority of the power settings. This was expected with the introduction of the HF acoustic source at 1.174 MHz, giving rise to fundamental and harmonic signatures [as seen by Figs. 3(a)–3(c)]. Interestingly, glycerol demonstrated the greatest increase in acoustic pressure ( $P_{\text{RMS}}$ ) under the DF setup for 20% and 60% input power [Fig. 2(d)], 180% and 97% increase, respectively]. For DIW, EtOH, and DIW:EtOH, the pressure percentage increases from a LF to DF setup for the  $P_{\text{RMS}}$  were measured to be 36%, 54%, and 44% (at 20% input power) and 27%, 19%, and 11% (at 60% input power), respectively (refer to the [supplementary material](#) Table S4). The combination of

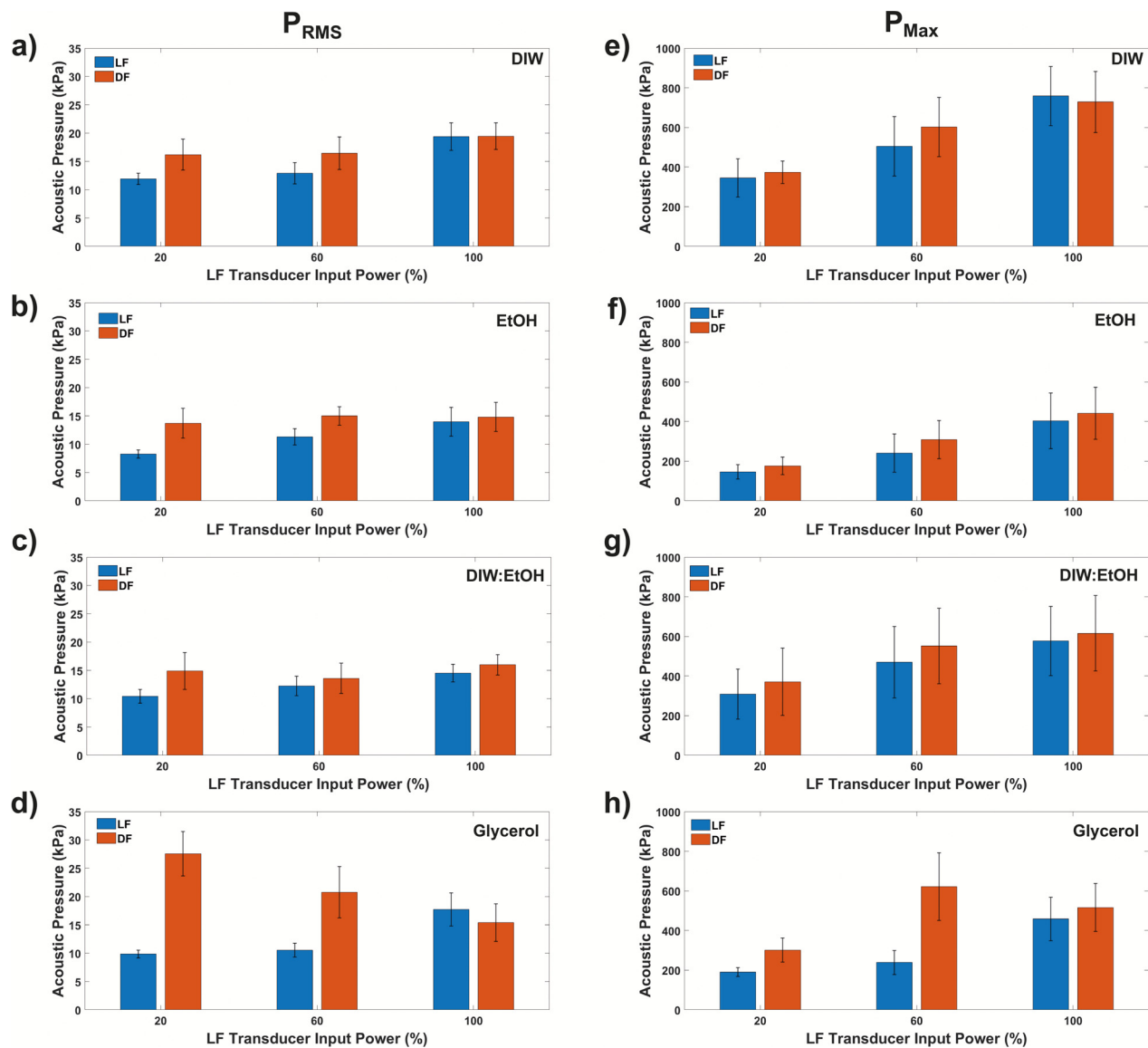


**FIG. 2.** Acoustic pressure measurements for frequency setups LF and DF. (a)–(d)  $P_{\text{RMS}}$  and (e)–(h)  $P_{\text{Max}}$ . The acoustic intensity ( $\times 10^{-6} \text{ W/m}^2$ ) corresponding to the sonication input powers for DF is as follows: DIW: 363 (20%), 1070 (60%), and 1636 (100%); EtOH: 359 (20%), 925 (60%), and 1349 (100%); DIW:EtOH: 504 (20%), 24 (60%), and 1212 (100%); glycerol: 1084 (20%), 1175 (60%), and 3272 (100%).



the two frequencies is likely to increase acoustic pressure by promoting additional bubble activity, hence, greater intensity detected by the FOH. This enhancement of cavitation activity under a multifrequency source has been previously reported in Ref. 19 and 21. For the case of solely using the HF source, sufficient cavitation is not generated at low input powers to be of use in many sono-processes, as noted for the exfoliation of graphite in Ref. 11 (also refer to the [supplementary material](#), Figs. S1 and S2 and Table S3). However, acoustic pressures are in the same range of those generated by the LF source due to the calibration sensitivity of the FOH being in the MHz range (1–30 MHz) with contributions mainly from the fundamental frequency of the HF source at 1.174 MHz and the corresponding harmonics. The generated spectrum has no evidence of transient cavitation activity being present. Hence, we decided to present only the cases of LF and DF where cavitation is developed as captured by the high-speed camera and the corresponding spectra.

The pressure plots demonstrate that the enhancement of cavitation between the LF and DF setups reduces when increasing input power (Fig. 2). The percentage difference between the frequency setups at 100% input power was much smaller than that of 20% and 60% input powers. This is likely due to the LF source gaining prominence and generating larger bubbly clouds, therefore, increasing cavitation shielding, including suppressing the incident wave from the membrane transducer leading to the reduced contribution of the DF setup. Interestingly, despite PRMS having an upward trend with input power for the LF case in Glycerol, when the DF setup is activated the  $P_{RMS}$  trend decreases. The  $P_{RMS}$  obtains the maximum pressure value (28 kPa) among all liquid cases at 20% input power in the DF configuration, followed by a gradual decay when increasing the LF power [Fig. 2(d)]. Glycerol's significant pressure increase in the DF setup

may be a consequence of its physical properties. The viscosity of glycerol is much greater than the other investigated solvents. A possible explanation may lie in the contribution from the incident wave (at 1.174 MHz) that propagates in the bulk liquid without being disrupted by the cavitation cloud (due to weak cavitation zone development at that power setting) in addition to harmonics and the long lifespan of bubbles in glycerol as explained in Ref. 1. Due to their tiny size, these HF bubbles are unlikely to collapse in such a viscous liquid.<sup>1</sup> Hence, the liquid is populated by tiny bubbles that tend to vigorously vibrate rather than collapse, overimposed to the emissions from the fundamental frequency as well as the main cavitation cloud (confined under the probe), which raises the overall pressure and cavitation noise at the MHz range [see Figs. 3(a)–3(c), green line]. However, when the LF input power increases (meaning a larger cavitation zone and cloud penetration depth with more collapses and associated SWs, although more shielding and cushioning of the intensity of the SWs on top of the acoustic damping), these tiny bubbles suppress the signal as opposed to amplifying it, due to blocking the propagation of the incident wave [notice the suppression of the fundamental peak in Figs. 3(b) and 3(c)]. Therefore, cavitation emissions from vigorously oscillating bubbles/clouds and SWs are suppressed (note the HF remains the same at 50% and, thus, the population of the bubbles). It is possible that these bubbles are captured within the parcel of liquid that is formed under the cavitation zone (as previously explained and discussed),<sup>1,25</sup> absorbing the powerful shock while their vibrating emissions are blocked without being able to reach the sensor. Hence, a trade-off exists between the size of the cavitation zone from the LF source and the bubbles from the HF source. When the cavitation zone is small (i.e., 20% input power), there is less shielding and acoustic emissions, and propagating SWs reach the sensor, further amplified by

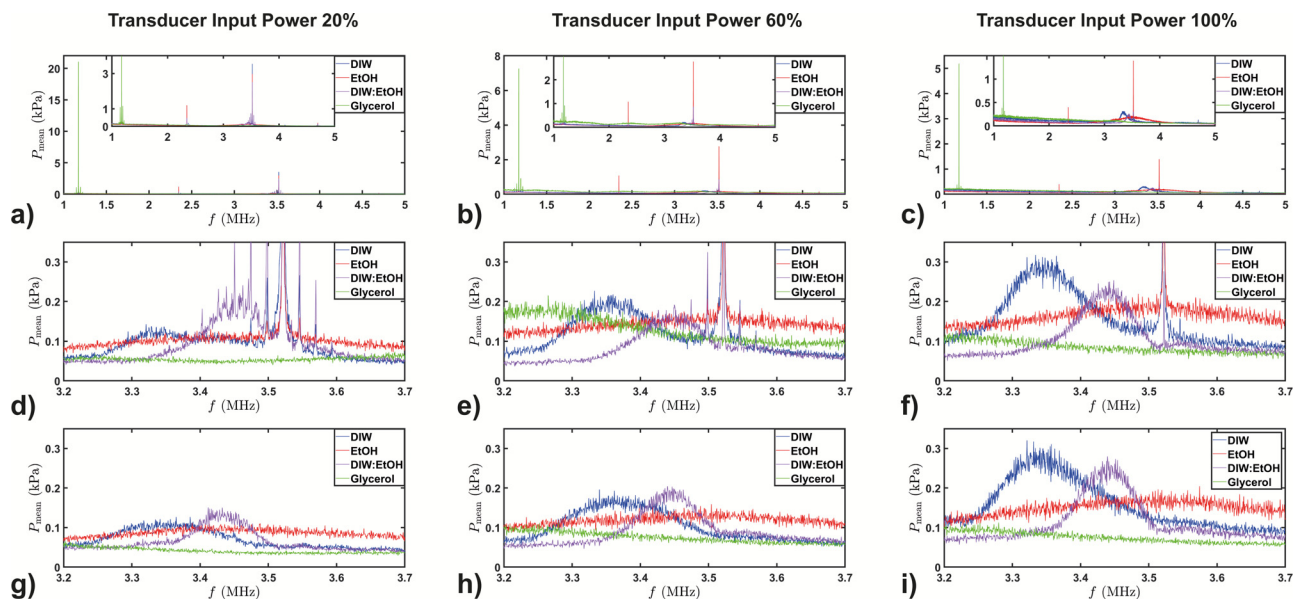


**FIG. 3.** Acoustic spectra showing DF and LF setups for each solvent, over an averaged acoustic pressure. (a)–(c) Full DF spectra for 20%, 60%, and 100% input powers, respectively. (d)–(f) DF spectra displaying the SW peak range ( $\sim 3.2$ – $3.7$  MHz) for 20%, 60%, and 100% input power, respectively. (g)–(i) LF spectra displaying the SW peak range ( $\sim 3.2$ – $3.7$  MHz) for 20%, 60%, and 100% input power, respectively. Note that the spectra range shows only between 1 and 5 MHz as at higher frequencies, the magnitude of the harmonics becomes negligible, and only low level broadband noise is generated (refer to the [supplementary material](#), Fig. S2).

the oscillating HF bubbles in the vicinity. Alternatively, when the LF cavitation zone increases (i.e., 100% input power), SW emissions dominate the pressure field, whereas the HF bubbles play a significantly smaller role, and their contribution to the overall spectrum is diminished [this is also apparent from Fig. 2(d) where the pressure level for both setups is almost the same, implying the insignificant role of the HF source at that input power from the LF]. This is likely why the  $P_{\text{Max}}$  pressure plot for glycerol [Fig. 2(h)] has an increasing trend (indicating a dominant SW pressure field as mentioned in Sec. II), whereas the  $P_{\text{RMS}}$  decreases with input power [Fig. 2(d)].

As previously mentioned, the FOH is primed to detect SWs (which are generally responsible for generating the largest acoustic emissions); hence, the  $P_{\text{Max}}$  plots are indicative of the inertial cavitation contribution. The  $P_{\text{Max}}$  acoustic pressures all gradually increase with input power (as more SWs are generated due to populated bubbly structures), and interestingly, with the introduction of the HF membrane, these pressures are further increased (with most cases between 5% and 30%), with larger increases in glycerol. This indicates that the DF mode improves the pressure magnitude of SWs by amplifying their intensity or by overimposing emissions (in the MHz range) by the tiny vigorously oscillating bubbles as shown previously.<sup>1</sup>

Figures 2(e)–2(h) demonstrate that the DF setup again enhances the cavitation intensity (other than DIW at input 100% power that slightly dropped, indicating contribution of shielding from the numerous bubbles). However, these plots reveal less of a pressure increase between the LF and DF setups, overall, compared to the  $P_{\text{RMS}}$  plots [Figs. 2(a)–2(d)]. We can attribute this phenomenon to the bubble dynamics of the HF source. The HF transducer membrane (1.174 MHz) does not produce transient cavitation, but rather tiny rapidly oscillating cavitation bubbles (i.e., stable cavitation, observed later in Sec. III B); hence,  $P_{\text{Max}}$  values demonstrate less of a difference. It does, however, indicate that the addition of the HF source promotes more transient collapses, as speculated previously in Ref. 38, plus further contribution to the spectrum from the vigorously oscillating bubbles, as, for example, shown in Fig. 3(a) for DIW:EtOH (see multiple spikes generated in the range of 1–4 MHz) and EtOH [cavitation noise increase, Figs. 3(b) and 3(c)]. This was more prominent for EtOH. It is known that EtOH has a higher tendency to nucleate bubbles, thus giving rise to prominent peaks at MHz frequencies due to long-lived vigorously oscillating bubbles,<sup>1</sup> increasing the cavitation zone and, therefore, generating larger measured maximum pressure readings.

Analysis of the DF acoustic spectra for all input powers [Figs. 3(a)–3(c)] shows the first harmonic (1.174 MHz) to be the most prominent, with glycerol significantly standing out (corresponding to the pressure measurements in Fig. 2). This is probably related to the formation of well-defined standing waves compared to other liquids due to the high viscosity, confined cavitation zone, and smaller amount of HF bubbles, which feature a lesser proclivity to nucleate in glycerol, and thus, they do not destruct the nodes/antinodes. Interestingly, the second and third harmonics for glycerol were largely suppressed, indicating that glycerol's driving frequency giving rise to its large measured pressures ( $P_{\text{RMS}}$ ) is a consequence of the fundamental frequency of the HF transducer (as previously discussed). The prominence of these HF peaks for glycerol and EtOH is also consistent with the larger percentage increase in  $P_{\text{RMS}}$  pressure measurements [Figs. 2(b) and 2(d)]. We also observe ultra-harmonics around the three HF harmonics [1.174, 2.347, and 3.522 MHz, Figs. 3(a)–3(c)] insets for DIW, EtOH, and

DIW:EtOH, respectively. Interestingly, these ultra-harmonics manifest at 24 kHz intervals around the HF peaks, perhaps an indication that they are regulated by the LF source. To the best of our knowledge, this is the first time this phenomenon has been noticed and will require further investigation in the future.

Comparing the SW peak [Figs. 3(d)–3(i)], we observed larger peaks for the DF setups [Figs. 3(d)–3(f)]. Particularly, DIW and DIW:EtOH at 20% and 60% input power demonstrate the largest increase in this peak, corresponding with the  $P_{\text{Max}}$  pressure readings (Fig. 2), again, indicating the increased prominence of transient cavitation effect using a DF setup. At 100% input power [Figs. 3(e), 3(f), 3(h), and 3(i)], a larger SW peak is less evident for DIW and DIW:EtOH compared to the LF setup (in confirmation with Fig. 2). This may also be in line with a larger contribution of shielding from the numerous bubbles at 100% input power using the DF setup. For EtOH and glycerol, this peak is not evident and appears as noise. It has been previously noted that this peak has a lesser tendency to manifest in these liquids, possibly consequential to attenuation of the wave, whereby acoustic damping occurs from the highly viscous glycerol<sup>25</sup> and also seen in Ref. 39. For EtOH, the lower speed of sound (compared to the other liquids) generates quicker decaying SWs; therefore, the SW peak becomes imperceptible (above noise). The large vapor pressure of EtOH is also a contributing factor to the absence of this peak for both DF and LF setups, decreasing the tendency for bubble collapse, therefore, giving prominence to the harmonic peaks via additional rapid bubble oscillation.<sup>1</sup> The SW peak was also observed to shift upwards in frequency for DIW:EtOH, aligning with a faster speed of sound propagating in the liquid as previously discussed in Refs. 25 and 40.

Interestingly, we observe that these humps of DIW:EtOH at 20% input power [Fig. 3(d)] are overimposed with acoustic emissions of oscillating bubbles evidenced by the sharp secondary peaks across the hump, indicating the presence of the “mist” cavitation with tiny oscillating bubbles as seen in Refs. 1 and 25. The occurrence of these high intensity peaks in the high frequency domain of the spectra can be correlated with linear pulsations of resonating tiny bubbles that are also in line with the Minnaert equation,<sup>41</sup> i.e., a peak at 3.5 MHz corresponds to a resonance radius of  $\sim 1 \mu\text{m}$ . This observation demonstrates the benefits of this liquid combination for producing nanomaterials, where these active tiny bubbles may be a key factor for quality exfoliation as previously seen in Ref. 26.

## B. Shadowgraphic high-speed imaging

In light of the acoustic pressure measurements, high-speed camera imaging was used to elucidate bubble dynamics for the selected liquids providing qualitative analysis. The behavior and development of cavitation under different frequency setups were investigated to observe what effect the HF transducer had on the liquids. Initial observations were taken for DIW as a reference liquid in Fig. 4, followed by the other studied liquids (Fig. 4). The HF setup produced no cavitation cloud (it should be noted that observations were made  $\sim 75 \text{ mm}$  from the surface of the membrane due to the design of the transducer). Due to the slow motion of the HF induced bubbles while having the camera recording at 1 Mfps [Fig. 3(a)], it was not feasible to capture their movement (as they appeared to be stationary). However, standing waves from the membrane were recorded, as indicated by the red arrows in Fig. 4(a) (and was also the case for the other investigated

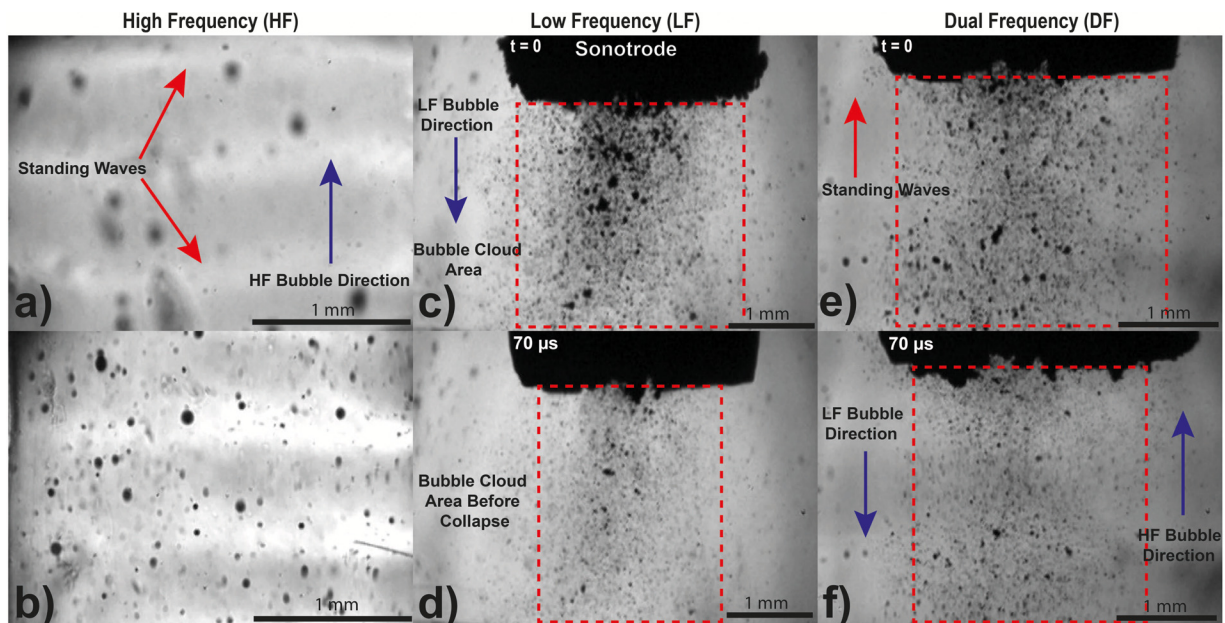


**FIG. 4.** Representative frames selected from multiple high-speed image sequences showing three ultrasonic frequency setups for DIW: (a) and (b) HF; (c) and (d) LF; (e) and (f) DF. (a) The HF set to 1174 kHz producing pressure nodes and antinodes (shadowgraphic imaging at 1 Mfps). (b) The same conditions but at the lower frame rate of 10 kfps, whereby the slower moving HF induced bubbles (compared to the LF induced bubbles) can be captured in motion. (c) The LF transducer during the formation of a bubble cloud (1 Mfps). (d) The LF transducer just before the same cloud collapses, 70  $\mu$ s after (c) (1 Mfps). (e) The DF setup during the formation of a bubble cloud (1 Mfps). (f) The DF setup just before the same cloud collapses, 70  $\mu$ s after (e) (1 Mfps). Note scale bar is at 1 mm. Multimedia views: <https://doi.org/10.1063/5.0136469.1>; <https://doi.org/10.1063/5.0136469.2>

solvents; EtOH, DIW:EtOH, and glycerol). By reducing the frame rate [Fig. 4(b), Multimedia view, 10 kfps], we were able to see through the camera footage with the field of view now populated with myriads of active bubbles. The majority of the HF bubbles are non-transient (no bubble implosion) with vigorous oscillating motion observed and as expected and discussed in Sec. III A (note that the standing waves are far more evident in the video and should be watched in the Multimedia view). However, larger HF cavitation bubbles of about 100  $\mu$ m were observed to oscillate with as much change as  $\sim 43\%$  of their overall diameter when shrinking/expanding, implying a vigorous oscillating behavior (note that the specific size changes of smaller HF bubbles cannot be resolved due to camera limitations). In addition, HF bubble velocities were calculated in the range of  $\sim 0.02$ – $0.08$   $\text{ms}^{-1}$  for approximate bubble diameter sizes of 4–100  $\mu$ m (corroborating with previous experimental observations;<sup>42</sup> note that some larger bubbles derive from pre-existing large in size gas bubbles as liquids were not degassed).

Figures 4(c) and 4(d) show high-speed imaging for the LF induced cavitation bubbles and respective cavitation zone in DIW. The large bubble cloud formed under the sonotrode tip generated strong collapses of the cavitating clouds, producing high pressures. Figures 4(e) (Multimedia view) and 4(f) show the DF setup consisting of the LF sonotrode and HF transducer membrane; hence, both the bubble cloud and the HF standing waves are visible. One observation between the LF and DF setup was the size of the cavitation cloud. Figures 4(c) and 4(e) show a cloud of bubbles forming under the sonotrode. Just before the cloud is about to collapse [Figs. 4(d) and 4(f)], the DF setup is seen to retain a larger bubble cloud volume [Fig. 4(f)],

with an increase in  $\sim 9\%$  in size. It is likely that these tiny bubbles are difficult to collapse due to their small size and surface tension; therefore, they tend to remain suspended in the liquid medium, thus retaining an active cavitation zone. Due to their long lifespan, the HF bubbles have time to grow and reach resonance size (due to rectified diffusion<sup>43</sup>) associated with LF transducer (around 100  $\mu$ m in radius) or merge into clouds, therefore becoming unstable and thereafter collapsing. Therefore, the DF setup retains a larger active cavitation zone, increasing the propensity of SW generation due to more bubble cloud collapses [also in-line with the larger measured  $P_{\text{Max}}$  values in Figs. 2(e)–2(h) and qualitatively seen in multimedia recordings corresponding to Figs. 4 and 5 where SW generation is more evident]. The HF bubbles play an active role in replenishing cavitation nuclei and, in turn, increasing the cavitation zone under the sonotrode tip (shown later in Fig. 6 schematic). Interestingly, the larger cavitation zone is also formed at the edges under the sonotrode tip in the DF mode, demonstrating additional nucleation of cavitation bubbles [Fig. 4(f)]. A larger cavitation zone generates stronger collapses complemented by numerous SW emissions. Previous research has suggested that small bubbles generated in the HF field nucleate cavitation bubbles in the LF cavitation zone.<sup>44</sup>

Shadowgraphic imaging of the remaining liquids (Fig. 5) reinforced these observations. EtOH under the DF setup was shown to produce a larger range of satellite bubbles (bubble fragments or secondary bubbles that move or form away from the sonotrode tip) that oscillated more rapidly, with a 57% more contraction from their maximum size than their LF counterpart [Figs. 5(a1–2)–5(b1–2)], Multimedia view]. This enhanced bubble oscillation also corroborates



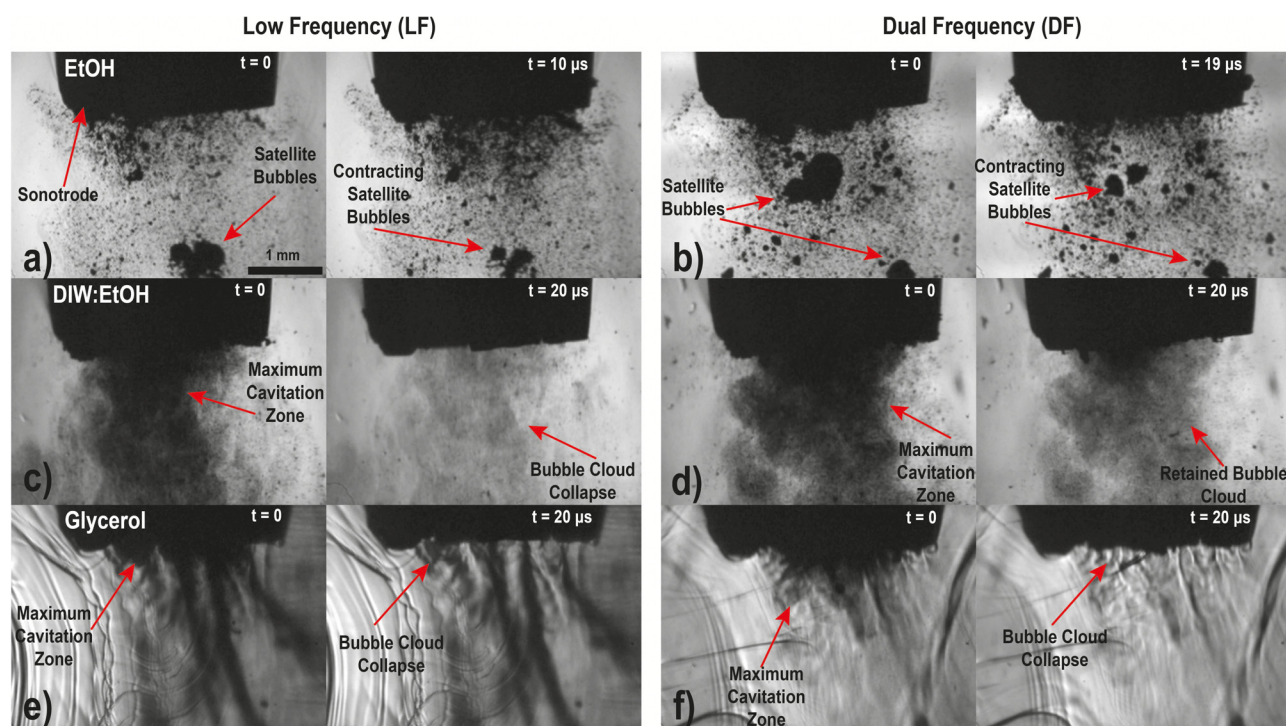


**FIG. 5.** Representative frames selected from multiple high-speed image sequences showing the difference between two ultrasonic frequency setups; (a) EtOH, showing the cavitation zone and oscillating motion of satellite bubbles under the LF source. (b) EtOH, showing the cavitation zone and oscillating motion of satellite bubbles under the DF source. (c) DIW:EtOH, showing the maximum cavitation zone and during cloud collapse for the LF source. (d) DIW:EtOH, showing the maximum cavitation zone and during cloud collapse for the DF source. (e) Glycerol, showing the maximum cavitation zone and cloud collapse for the LF source. (f) Glycerol, showing the maximum cavitation zone and cloud collapse for the DF source. Time duration between images is shown for each sequence. Imaging was taken at 1 Mfps. Note scale bar is at 1 mm. Multimedia views: <https://doi.org/10.1063/5.0136469.3>; <https://doi.org/10.1063/5.0136469.4>

with the pressure data presented in Fig. 2(b). The case of DIW:EtOH also demonstrated retention of more bubbles in the cavitation zone (notice that the cloud mist retains formation) during the collapse of the bubble cloud for the DF setup [Fig. 5(c1–2)] compared to the LF setup [Fig. 5(d1–2)]. For the case of glycerol [Figs. 5(e1)–5(f2)], significant observations of the cavitation zone were limited using the high-speed camera. However, image analysis did reveal an increase in the cross-sectional area of the cavitation zone under DF ultrasound. Interestingly, analysis of the cavitation zone enhancement of the liquids coincided with the pressure measurements using the FOH (Fig. 2). These percentage increases in cross-sectional area were calculated for glycerol, EtOH, DIW:EtOH, and DIW to be 17.2%, 16.5%, 11.9%, and 8.7%, respectively (refer to the [supplementary material Table S5](#)). Apart from glycerol where viscosity is the dominant property, the surface tension values of the studied liquids follow the same trend. The lower surface tension produces a higher propensity to nucleate bubbles, hence, increasing the cavitation zone, a phenomenon also delineated under the influence of a DF setup.

We can, therefore, summarize the most salient observations of the DF setups to demonstrate bubble clusters and LF bubbles moving away from the sonotrode tip to sustain longer lifecycles while rapidly oscillating. By analyzing the LF and DF image sequences (Fig. 5) and corresponding video recordings, we observed that these satellite bubbles/fragments of bubbles appear to have a higher tendency to remain

in the cavitation zone, whereby the interaction with traveling SWs re-energizes them, promoting growth and further collapses (that is also in line with recent observations<sup>45</sup>). In the DF scenario, we also noticed that the size and oscillating motion of the bubble fragments are sustained for longer periods of time under the HF pressure field [most noticeable in EtOH Fig. 5(b1–2)], in addition to higher probability of bubble coalescence. The larger cavitation zone and additional satellite bubbles are likely a contributing factor for the larger measured acoustic pressures by the FOH [Figs. 2(e)–2(h)], detecting more SWs from more transient cavitation collapses and overall cavitation activity. These observations are graphically portrayed in the schematic, whereby the LF source [Fig. 6(a)] generates a smaller cavitation zone with lesser secondary cavitation such as oscillating satellite bubbles. Additionally, it is also evident that the spatial distribution of the satellite bubbles formed from the cavitation cloud increased under the influence of the HF transducer being activated as merging with tiny HF bubbles occurs sustaining a larger/expanding active cavitation zone [Fig. 6(b)] and demonstrated by the high-speed camera, Figs. 4 and 5].

### C. Synchronized high-speed imaging and acoustic pressure measurements

Figure 7 shows a series of images and waveforms obtained using a synchronization technique of high-speed recordings with real-time

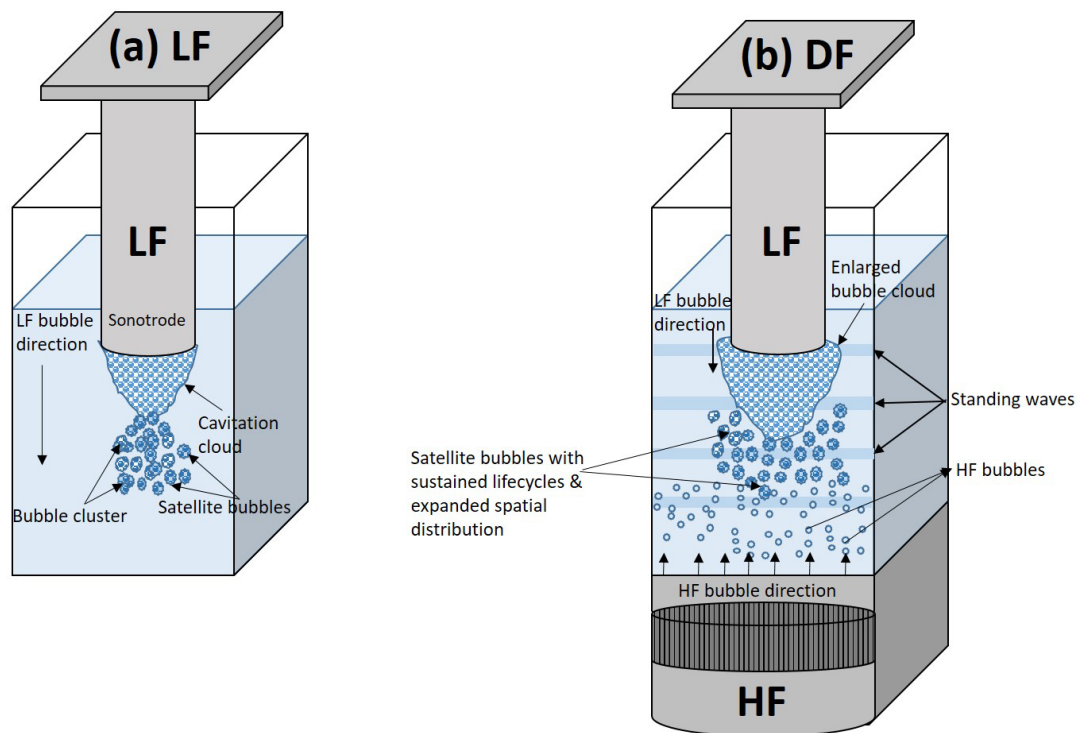


**FIG. 6.** Schematic of cavitating environment under (a) the sonotrode, producing LF cavitation bubbles, and (b) the DF setup, combining the LF and HF cavitation bubbles for DIW. (a) The sonotrode produces a cavitation zone, mostly directly under the tip. (b) The combination of the two frequencies to enhance the cavitation activity. The cavitation zone under the sonotrode tip is expanded, with the lifecycle of the satellite bubbles extended, in addition to their increased spatial distribution in the liquid medium. HF bubbles are seen to oscillate with much smaller radii, moving upwards, in the opposite direction of the sonotrode, mixed with the satellite bubbles and suspended clouds, replenishing cavitation nuclei and to facilitate enlargement of the cavitation zone under the sonotrode tip.

acoustic pressure measurements (Fig. 7, for 20% input power). Initial observations reveal that DIW [Fig. 7(a)] appears the least enhanced with the addition of the HF transducer. The largest difference between the LF and DF setup is demonstrated by glycerol, followed by EtOH and DIW:EtOH [Figs. 7(b)–7(d)], coinciding with the previously measured pressure increases (Fig. 2). An increase in cavitation noise is evident for all the DF cases, where, particularly, DIW and DIW:EtOH [Figs. 7(a) and 7(c)], respectively, induce more SWs (indicated by the sharp peaks), which generate approximately 2.5 times larger peaks than for EtOH and glycerol [Figs. 7(b) and 7(d), respectively]. Glycerol is shown to generate multiple bubble collapses [Fig. 7(d)]; however, due to high viscosity of the liquid, the SW power rapidly diminishes (reaching up to  $\sim 400$  kPa) and produces sparse individual peaks. EtOH generates even fewer individual peaks [Fig. 7(b)] with less cavitation intensity (a few reaching up to  $\sim 200$  kPa) indicating less SWs, with a fluctuating pressure time plot. This may be a consequence of prominent vibrating bubble oscillation, which is non periodic inducing a non-consistent pressure time domain. The plots of Figs. 7(b) and 7(d) especially indicate that the addition of the HF transducer predominantly enhances rapid bubble oscillation, as opposed to increasing transient cavitation (whereby bubble collapses would produce more prominent individual large pressure peaks indicative of SW generation). For instance, the largest recorded pressure peaks are over 1000 kPa for the DF DIW and DIW:EtOH setups [Figs.

7(a) and 7(c)], whereas more uniform pressure distributions (smaller difference between bulk pressures and maximum peaks) are evident for the DF EtOH setup [Fig. 7(b)], and especially, for the DF glycerol setup [Fig. 7(d)], both generally generate less than 400 kPa peaks and demonstrate a prominent acoustic contribution from the fundamental frequency [shown in Figs. 3(a)–3(c)]. It should be noted that SW energy as evidenced by the negative and positive pressure time traces (measured by the FOH) is dissipated as broadband noise in the frequency domain, with only a very small portion (as explained previously<sup>18</sup>) contributing to this small rise (a few kPa) at  $\sim 3.2$ – $3.6$  MHz as shown in Figs. 3(d)–3(i).

High-speed imaging using the Photron camera (non shadow-graphic imaging) was unable to capture the standing waves propagating from the HF transducer. Hence, the difference between the insets (Fig. 7) of the LF and DF setups is harder to distinguish. However, the basic pattern for both setups demonstrates a growing cavitation cloud over the first 10 ms [insets (1)–(4)], followed by a stabilized period with a smaller cavitation zone [insets (5) and (6)]. As previously reported, EtOH produces a larger cavitation cloud than DIW, and the mixture of DIW:EtOH produces a mist like cavitation, which extends the cavitation zone with smaller dispersed cavitation bubbles.<sup>25,26</sup> Glycerol's cavitation zone is localized at the sonotrode tip in both frequency setups with a more homogeneous waveform (indication of continuous contribution from the incident wave) and pressure surges

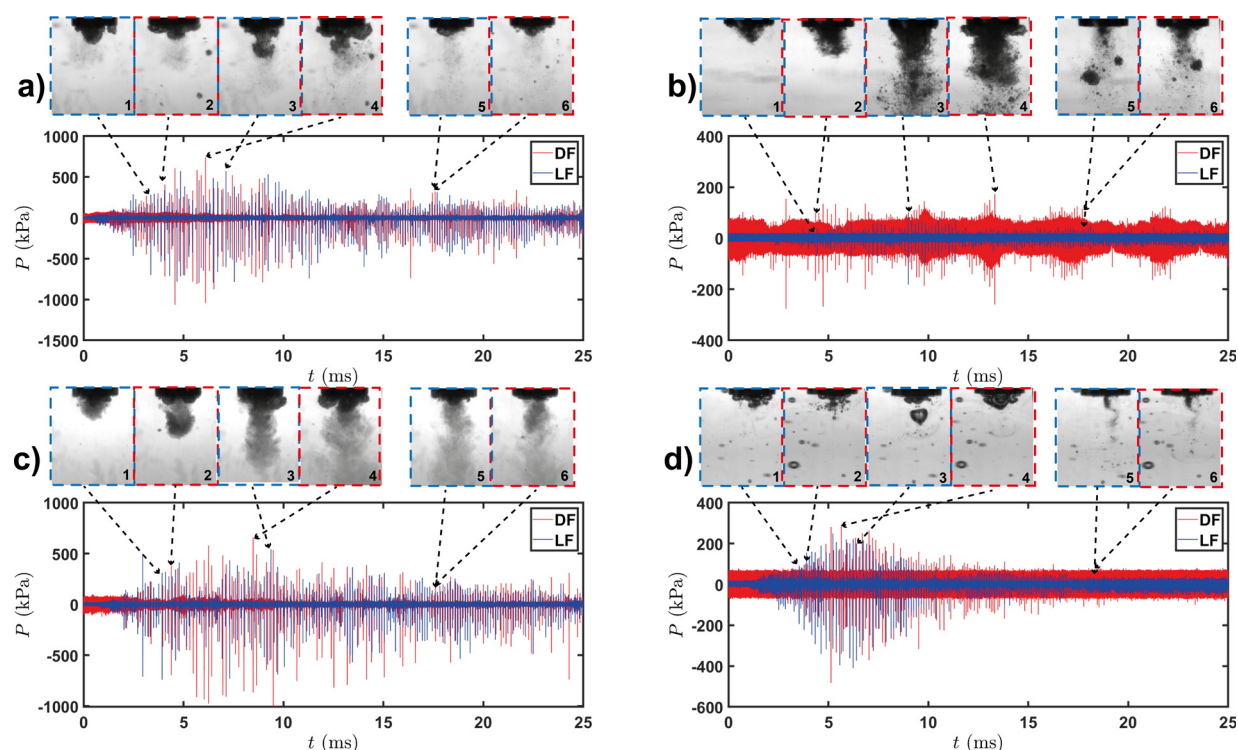


**FIG. 7.** Synchronized high-speed images (insets) with acoustic pressure plots for each studied liquid: (a) DIW, (b) EtOH, (c) DIW:EtOH, and (d) glycerol, whereby the DF (red) and LF (blue) data are plotted together for comparison. The period of 25 ms is recorded once the LF source is activated. The insets display four representative moments (indicated via the arrows, blue boxed images are LF, while red boxed images are DF) of the developing bubble dynamics for each solvent: (1) initial activation of the sonotrode for the LF setup, (2) initial activation of the sonotrode for the DF setup, (3) maximum cavitation cloud before collapse for the LF setup (thereafter, a large corresponding pressure spike is induced), (4) maximum cavitation cloud before collapse for the DF setup, (5) stabilized cavitation period for the LF setup, and (6) stabilized cavitation period for the DF setup. Imaging was taken at 100 kfps, with intensity measured via a FOH and converted to acoustic pressure. The transducer input power was set to 20%.

from the DF setup. The higher viscosity of glycerol and the high vapor pressure of EtOH, both inhibiting bubble collapse, may promote bubble oscillation under the DF setup. This may explain why these two solvents are subject to an increase in cavitation intensity ( $P_{RMS}$  for EtOH and  $P_{Max}$  for glycerol) when combining both a LF and HF source. DIW:EtOH demonstrates an enhanced pressure field from LF to DF (43%) and an enlarged cavitation zone (12%) populated via tiny microbubbles in the form of cavitation mist, which strongly supports why this combination of liquids under a DF source is favorable for exfoliation as observed previously.<sup>19</sup> Additionally, the formation of these tiny cavitation bubbles may penetrate in-between the layers of layered materials, therefore, facilitating exfoliation and agreeing with the results reported elsewhere.<sup>26</sup>

#### IV. CONCLUSIONS

The benefits of using a DF transducer setup were recently demonstrated for the production of 2D nanomaterials in the studied liquids.<sup>27</sup> This work took the next step and presented analysis into a DF ultrasonic system (24 kHz and 1.174 MHz), providing insightful information on the reasons behind this advancement. Bubble dynamics, acoustic pressures, spectra, and generated SWs were elucidated and compared with a single (standard setup), LF

sonotrode source (24 kHz) for various liquids (DIW, EtOH, DIW:EtOH, and glycerol). This was demonstrated using ultra-high-speed imaging, showing how the combination of a LF and HF source improved cavitation activity and enhanced the cavitation zone. In general, the DF setup generated greater acoustic pressures (up to 180% increase). These data were re-enforced with the aid of synchronized high-speed imaging and acoustic pressure measurements that showed bubble dynamics in real-time with acoustic emissions. The selected image sequences also showed an increased size of the cavitation zone directly under the sonotrode tip (9%–17% increase). In addition, the DF setup increased the spatial distribution of satellite bubbles and bubble clusters from the LF source while extending their lifecycles by maintaining a larger cavitation zone [Figs. 4(e), 4(f), and 5(d)], therefore increasing the propensity of more powerful bubble collapses and, hence, more SW emissions. Furthermore, utilizing the DF setup also promoted vigorous bubble oscillations due to many smaller additional cavitation bubbles unable to collapse, hence enhancing the overall cavitation activity. This was particularly the case for DIW:EtOH liquid that was recently found to be a suitable solvent for cavitation exfoliation of graphene.<sup>19,26</sup> The analysis and observations from this study can contribute to developing and validating multifrequency numerical



models, in addition to optimizing and controlling a cavitation processing method for multifrequency systems.

## SUPPLEMENTARY MATERIAL

See the [supplementary material](#) for additional data acquisition, bubble dynamics calculations, and physical properties of investigated liquids.

## ACKNOWLEDGMENTS

This work was funded by the UK Engineering and Physical Sciences Research Council (EPSRC) to the project “Sustainable and industrially scalable ultrasonic liquid phase exfoliation technologies for manufacturing 2D advanced functional materials” (EcoUltra2D) with the Grant Nos. EP/R031665/1, EP/R031401/1, EP/R031819/1, and EP/R031975/1.

## AUTHOR DECLARATIONS

### Conflict of Interest

The authors have no conflicts to disclose.

## Author Contributions

**Justin Morton:** Conceptualization (equal); Data curation (equal); Investigation (equal); Visualization (equal); Writing – original draft (equal); Writing – review & editing (equal). **Iakovos Tzanakis:** Conceptualization (equal); Formal analysis (equal); Funding acquisition (equal); Writing – review & editing (equal). **Mohammad Khavari:** Conceptualization (equal); Data curation (equal); Software (equal). **Abhinav Priyadarshi:** Data curation (equal); Investigation (equal); Visualization (equal). **Amanpreet Kaur:** Data curation (equal). **Nicole Grobert:** Funding acquisition (equal). **J. Mi:** Funding acquisition (equal). **Kyriakos Porfyrakis:** Funding acquisition (equal). **Paul Prentice:** Data curation (equal); Formal analysis (equal); Writing – review & editing (equal). **Dmitry Eskin:** Funding acquisition (equal); Writing – review & editing (equal).

## DATA AVAILABILITY

The data that support the findings of this study are available from the corresponding authors upon reasonable request.

## REFERENCES

1. Tzanakis, G. S. B. Lebon, D. G. Eskin, and K. A. Pericleous, “Characterizing the cavitation development and acoustic spectrum in various liquids,” *Ultrason. Sonochem.* **34**, 651–662 (2017).
2. M. S. Lucas, J. A. Peres, and G. L. Puma, “Advanced oxidation processes for water and wastewater treatment,” *Water* **13**(9), 1309 (2021).
3. K. S. Suslick and W. L. Nyborg, “ULTRASOUND: Its chemical, physical and biological effects,” *J. Acoust. Soc. Am.* **87**(2), 919 (1998).
4. T. J. Mason and A. Tiehm, *Advances in Sonochemistry*, Vol. 6 (Elsevier, 2001), p. 284.
5. F. Cavaliere, M. Zhou, and M. Ashokkumar, “The design of multifunctional microbubbles for ultrasound image-guided cancer therapy,” *Curr. Top. Med. Chem.* **10**(12), 1198–1210 (2010).
6. J. R. McLaughlan, S. Harput, R. H. Abou-Saleh, S. A. Peyman, S. Evans, and S. Freear, “Characterisation of liposome-loaded microbubble populations for sub-harmonic imaging,” *Ultrasound Med. Biol.* **43**(1), 346–356 (2017).
7. C. M. Schoellhammer *et al.*, “Ultrasound-mediated gastrointestinal drug delivery,” *Sci. Transl. Med.* **7**(310), 310ra168 (2015).
8. K.-V. Jenderka and C. Koch, “Investigation of spatial distribution of sound field parameters in ultrasound cleaning baths under the influence of cavitation,” *Ultrasonics* **44**(1), 44 (2006).
9. B. Zeqiri, M. Hodnett, and A. J. Carroll, “Studies of a novel sensor for assessing the spatial distribution of cavitation activity within ultrasonic cleaning vessels,” *Ultrasonics* **44**(1), 73–82 (2006).
10. A. Priyadarshi *et al.*, “On the governing fragmentation mechanism of primary intermetallics by induced cavitation,” *Ultrason. Sonochem.* **70**, 105260 (2021).
11. A. Tyurnina *et al.*, “Ultrasonic exfoliation of graphene in water: A key parameter study,” *Carbon* **168**, 737–747 (2020).
12. X. Gu *et al.*, “Method of ultrasound-assisted liquid-phase exfoliation to prepare graphene,” *Ultrason. Sonochem.* **58**, 104630 (2019).
13. P. Turner, M. Hodnett, R. Dorey, and J. D. Carey, “Controlled sonication as a route to *in-situ* graphene flake size control,” *Sci. Rep.* **9**(1), 1–8 (2019).
14. O. Supponen, D. Obreschkow, P. Kobel, M. Tinguely, N. Dorsaz, and M. Farhat, “Shock waves from nonspherical cavitation bubbles,” *Phys. Rev. Fluids* **2**(9), 093601 (2017).
15. J. A. Morton *et al.*, “New insights into sono-exfoliation mechanisms of graphite: *In situ* high-speed imaging studies and acoustic measurements,” *Mater. Today* **49**, 10–22 (2021).
16. K. Johnston *et al.*, “Periodic shock-emission from acoustically driven cavitation clouds: A source of the subharmonic signal,” *Ultrasonics* **54**(8), 2151–2158 (2014).
17. K. Johansen, J. H. Song, K. Johnston, and P. Prentice, “Deconvolution of acoustically detected bubble-collapse shock waves,” *Ultrasonics* **73**, 144–153 (2017).
18. M. Khavari, A. Priyadarshi, A. Hurrell, K. Pericleous, D. Eskin, and I. Tzanakis, “Characterization of shock waves in power ultrasound,” *J. Fluid Mech.* **915**, R3 (2021).
19. A. V. Tyurnina *et al.*, “Environment friendly dual-frequency ultrasonic exfoliation of few-layer graphene,” *Carbon* **185**, 536 (2021).
20. L. Qin *et al.*, “Ultrafast synchrotron x-ray imaging and multiphysics modelling of liquid phase fatigue exfoliation of graphite under ultrasound,” *Carbon* **186**, 227–237 (2022).
21. R. Feng, Y. Zhao, C. Zhu, and T. J. Mason, “Enhancement of ultrasonic cavitation yield by multi-frequency sonication,” *Ultrason. Sonochem.* **9**(5), 231–236 (2002).
22. G. Iernetti, P. Ciuti, N. V. Dezhkunov, M. Reali, A. Francescutto, and G. K. Johri, “Enhancement of high-frequency acoustic cavitation effects by a low-frequency stimulation,” *Ultrason. Sonochem.* **4**(3), 263–268 (1997).
23. K. M. Swamy and K. L. Narayana, “Intensification of leaching process by dual-frequency ultrasound,” *Ultrason. Sonochem.* **8**(4), 341–346 (2001).
24. S. Wang, B. Huang, Y. Wang, and L. Liao, “Comparison of enhancement of pentachlorophenol sonolysis at 20 kHz by dual-frequency sonication,” *Ultrason. Sonochem.* **13**(6), 506–510 (2006).
25. M. Khavari *et al.*, “Cavitation-induced shock wave behaviour in different liquids,” *Ultrason. Sonochem.* (unpublished).
26. J. A. Morton *et al.*, “An eco-friendly solution for liquid phase exfoliation of graphite under optimised ultrasonication conditions,” *Carbon* **204**, 434 (2022).
27. K. L. Ng *et al.*, “Direct evidence of the exfoliation efficiency and graphene dispersibility of green solvents toward sustainable graphene production,” *ACS Sustainable Chem. Eng.* **11**, 58–66 (2023).
28. A. O. Borode, N. A. Ahmed, and P. A. Olubambi, “Surfactant-aided dispersion of carbon nanomaterials in aqueous solution,” *Phys. Fluids* **31**(7), 071301 (2019).
29. K. E. Haddad, C. Aumnate, C. Saengow, M. A. Kanso, S. J. Coombs, and A. J. Giacomini, “Complex viscosity of graphene suspensions,” *Phys. Fluids* **33**(9), 093109 (2021).
30. G. Salussolia, C. Kamal, J. Stafford, N. Pugno, and L. Botto, “Simulation of interacting elastic sheets in shear flow: Insights into buckling, sliding, and reassembly of graphene nanosheets in sheared liquids,” *Phys. Fluids* **34**(5), 053311 (2022).
31. N. Brezhneva, N. V. Dezhkunov, S. A. Ulasevich, and E. V. Skorb, “Characterization of transient cavitation activity during sonochemical modification of magnesium particles,” *Ultrason. Sonochem.* **70**, PMC7786532 (2021).



- <sup>32</sup>I. Tzanakis, M. Hadfield, and I. Henshaw, "Observations of acoustically generated cavitation bubbles within typical fluids applied to a scroll expander lubrication system," *Exp. Therm. Fluid Sci.* **35**(8), 1544–1554 (2011).
- <sup>33</sup>N. Ouyang *et al.*, "Effect of slit dual-frequency ultrasonic emulsification technology on the stability of walnut emulsions," *Ultrason. Sonochem.* **82**, 105876 (2022).
- <sup>34</sup>Z. Zhang *et al.*, "Effect of dual-frequency ultrasound on the formation of lysinoalanine and structural characterization of rice dreg protein isolates," *Ultrason. Sonochem.* **67**, 105124 (2020).
- <sup>35</sup>B. Wang *et al.*, "Mechanism study of dual-frequency ultrasound assisted enzymolysis on rapeseed protein by immobilized Alcalase," *Ultrason. Sonochem.* **32**, 307–313 (2016).
- <sup>36</sup>C. Chaussy, W. Brendel, and E. Schmiedt, "Extracorporeally induced destruction of kidney stones by shock waves," *Lancet* **2**(8207), 1265–1268 (1980).
- <sup>37</sup>G. S. B. Lebon, I. Tzanakis, K. Pericleous, and D. Eskin, "Experimental and numerical investigation of acoustic pressures in different liquids," *Ultrason. Sonochem.* **42**, 411–421 (2018).
- <sup>38</sup>A. H. Barati, M. Mokhtari-Dizaji, H. Mozdarani, Z. Bathaie, and Z. M. Hassan, "Effect of exposure parameters on cavitation induced by low-level dual-frequency ultrasound," *Ultrason. Sonochem.* **14**(6), 783–789 (2007).
- <sup>39</sup>I. Tzanakis, M. Khavari, M. Titze, and D. G. Eskin, "Cavitation in thermoplastic melts: New insights into ultrasound-assisted fibre-impregnation," *Composites, Part B* **229**, 109480 (2022).
- <sup>40</sup>A. Kaur *et al.*, "Temperature as a key parameter for graphene sono-exfoliation in water," *Ultrason. Sonochem.* **90**, 106187 (2022).
- <sup>41</sup>M. Minnaert, "XVI. On musical air-bubbles and the sounds of running water," *London, Edinburgh, Dublin Philos. Mag. J. Sci.* **16**(104), 235–248 (2009).
- <sup>42</sup>G. S. B. Lebon, I. Tzanakis, K. Pericleous, D. Eskin, and P. S. Grant, "Ultrasonic liquid metal processing: The essential role of cavitation bubbles in controlling acoustic streaming," *Ultrason. Sonochem.* **55**, 243–255 (2019).
- <sup>43</sup>T. Leong, M. Ashokkumar, and S. Kentish, "The growth of bubbles in an acoustic field by rectified diffusion," in *Handbook of Ultrasonics and Sonochemistry* (Springer, 2016), pp. 69–98.
- <sup>44</sup>A. Brothie, R. Mettin, F. Grieser, and M. Ashokkumar, "Cavitation activation by dual-frequency ultrasound and shock waves," *Phys. Chem. Chem. Phys.* **11**(43), 10029–10034 (2009).
- <sup>45</sup>M. Petkovšek, M. Hočvar, and M. Dular, "Visualization and measurements of shock waves in cavitating flow," *Exp. Therm. Fluid Sci.* **119**, 110215 (2020).